INTERNATIONAL JOURNAL FOR NUMERICAL METHODS IN FLUIDS, VOL. 21, 1–13 (1995)

# NUMERICAL CALCULATION OF THE VISCOUS FLOW AROUND A PROPELLER SHAFT CONFIGURATION

KEON-JE OH

*Department of Mechanical Engineering, Kyungnam University, Wolyoung-Dong 449, Masan 631-701, South Korea*

AND

SHIN-HYOUNG KANG

*Department of Mechanical Engineering, Seoul National University, Shinrim-Dong, Seoul, South Korea*

## SUMMARY

A viscous flow simulation method is developed to calculate the flow around a marine propeller configuration and applications to propeller flow under uniform flow conditions are presented. The continuity and Reynolds-averaged Navier–Stokes equations are solved in a rotating co-ordinate system using the finite volume method. The turbulent Reynolds stresses are modelled by the modified $k$–$\varepsilon$ turbulence model to account for swirling flows. The general characteristics of propeller flow can be reasonably predicted in the slipstream of the propeller wake and the results of the circumferentially averaged velocity profiles show good agreement with experimental data. The tip vortex can be captured near the tip of the blade, but the strength of the vortex is weakly predicted in comparison with the measured one. The predictions of the boundary layer on the blade show reasonable agreement with measurements in the turbulent boundary layer region. However, the laminar and transitional boundary layers cannot be represented, because the flow is assumed to be turbulent in the calculation. The thrust and torque coefficients are adequately estimated in comparison with measured data for a wide range of advance coefficients.

KEY WORDS: propeller flow; Navier–Stokes equation; finite volume method; $k$–$\varepsilon$ turbulence model

## 1. INTRODUCTION

A propeller is a form of self-propulsion which produces thrust by the creation of lift as the flow passes through each blade of the propeller. In the propeller flow field a number of viscous flow phenomena can be identified, including blade and hub boundary layers, flow separation on the blade, viscous–inviscid interaction, hub and tip vortices, viscous wake, etc. Study of these viscous flow characteristics is essential for accurate prediction of the propulsion performance and for improving the propulsion efficiency. At present, most computational methods for calculating propeller flow are mainly based on potential flow theory with emperical corrections for viscous effects. In the case of a propeller operating in a uniform flow, inviscid flow calculations give reasonable results for the pressure and velocity distributions in the propeller flow field except in the boundary layer region on the blade and hub, because viscous effects are confined to a small region near the wall surface. However, when the propeller operates in the non-uniform flow of the viscous wake behind the stern, the flow field is greatly influenced by viscous effects and the flow is complicated by the propeller–hull interaction. In this case the inviscid flow assumption is not adequate and full viscous simulations involving the solution of the Navier–Stokes equations are needed to accurately predict the flow field.

Various numerical methods for viscous flow simulation have been developed and much work has been done on turbomachinery-type flow. For propeller flow, however, relatively little work has been

CCC 0271–2091/95/010001–13

*Received May 1994*
*Revised October 1994*

done and few results have been published. Stern *et al.*[1] presented a viscous flow approach for computation of the propeller–hull interaction using the finite analytic method. The viscous flow with a body force propeller is calculated in an interactive and iterative manner and the results show good agreement with circumferentially averaged measured data. However, this approach basically neglects circumferential variation in the flow variables and cannot show the flow features of propeller flow. Kim and Stern[2] and Kim[3] presented viscous simulation results for the idealized propeller with infinite-pitch rectangular blade and for a real propeller model respectively. These works show that the viscous flow method can simulate many of the general features of propeller flow. However, detailed investigations of the blade boundary layer, propeller wake and tip vortex are not included and the possibilities of the viscous flow method are not fully tested, because extensive comparisons between calculations and measurements were not made. With regard to the experimental study of propeller flow, very little information is available not only to understand the physical flow features but also to evaluate the numerical method. Jessup[4] carried out experiments on a propeller operating in a uniform flow and provided considerable information on the blade boundary layer, tip vortex and propeller wake. Hyun[5] performed experimental work on a propeller operating behind an axisymmetric body and presented an extensive set of experimental data in the propeller wake.

In the present study a viscous flow simulation method is developed to calculate the flow around a marine propeller configuration and calculations are made for the propeller flow model of Jessup[4]. The flow characteristics of the wake slipstream, blade boundary layer and tip vortex are investigated by the viscous flow method. Extensive comparisons between calculation results and experimental data are made to demonstrate the capability of the method to handle propeller flows.

## 2. GOVERNING EQUATIONS

The configuration of the rotating propeller in the uniform flow is shown in Figure 1. The governing equations for the incompressible, steady and turbulent flows are given by the continuity and Reynolds-

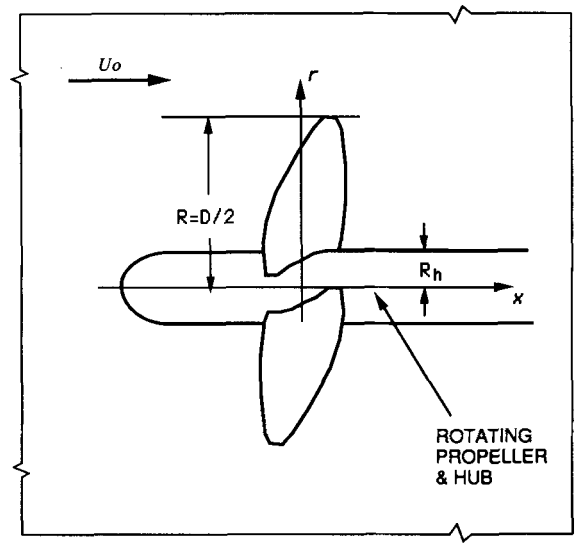


Figure 1. Configuration of flow domain and co-ordinate system around a propeller

Table I. $\phi$, $\Gamma_\phi$, and $S_\phi$ for governing equations

| $\phi$ | $\Gamma_\phi$ | $S_\phi$ |
|---|---|---|
| 1 | 0 | 0 |
| $U$ | $\nu_e$ | $-\frac{1}{\rho}\frac{\partial P}{\partial x}+\frac{\partial}{\partial x}\left(\nu_t\frac{\partial U}{\partial x}\right)+\frac{1}{r}\frac{\partial}{\partial r}\left(r\nu_t\frac{\partial V}{\partial x}\right)+\frac{1}{r}\frac{\partial}{\partial\theta}\left(\nu_t\frac{\partial W}{\partial x}\right)$ |
| $V$ | $\nu_e$ | $-\frac{1}{\rho}\frac{\partial P}{\partial r}+\frac{\partial}{\partial x}\left(\nu_t\frac{\partial U}{\partial r}\right)+\frac{1}{r}\left(r\nu_t\frac{\partial V}{\partial r}\right)+\frac{1}{r}\frac{\partial}{\partial\theta}\left(\nu_t\frac{\partial W}{\partial r}\right)-\frac{1}{r^2}\frac{\partial}{\partial\theta}(\nu_t W)\frac{2\nu_e}{r^2}\frac{\partial W}{\partial\theta}$ $-\nu_e\frac{V}{r^2}-\nu_t\frac{V}{r^2}+\frac{W^2}{r}+r\omega^2+2\omega W$ |
| $W$ | $\nu_e$ | $-\frac{1}{\rho r}\frac{\partial P}{\partial\theta}+\frac{\partial}{\partial x}\left(\frac{\nu_t}{r}\frac{\partial U}{\partial\theta}\right)+\frac{1}{r}\frac{\partial}{\partial r}\left(\nu_t\frac{\partial V}{\partial\theta}\right)+\frac{1}{r}\frac{\partial}{\partial\theta}\left(\frac{\nu_t}{r}\frac{\partial W}{\partial\theta}\right)-\frac{1}{r}\frac{\partial}{\partial r}(\nu_t W)+\frac{2}{r}\frac{\partial}{\partial\theta}\left(\frac{\nu_t}{r}V\right)$ $-\nu_e\frac{W}{r^2}+\frac{\nu_t}{r}\frac{\partial W}{\partial r}+\frac{\nu_e}{r^2}\frac{\partial V}{\partial\theta}+\frac{\nu}{r^2}\frac{\partial V}{\partial\theta}-\frac{VW}{r}-2\omega V$ |
| $k$ | $\frac{\nu_e}{\sigma_k}$ | $G-C_D\varepsilon$ |
| $\varepsilon$ | $\frac{\nu_e}{\sigma_\varepsilon}$ | $\frac{\varepsilon}{k}(C_1G-C_2\varepsilon)$ |

$$G=\nu_t\left\{2\left[\left(\frac{\partial U}{\partial x}\right)^2+\left(\frac{\partial V}{\partial r}\right)^2+\left(\frac{1}{r}\frac{\partial W}{\partial\theta}+\frac{V}{r}\right)^2\right]+\left(\frac{\partial U}{\partial r}+\frac{\partial V}{\partial x}\right)^2+\left(\frac{1}{r}\frac{\partial U}{\partial\theta}+\frac{\partial W}{\partial x}\right)^2+\left(\frac{1}{r}\frac{\partial V}{\partial\theta}+\frac{\partial W}{\partial r}-\frac{W}{r}\right)^2\right\}$$

$$\nu_e=\nu+\nu_t,\qquad \nu_t=C_\mu\frac{k^2}{\varepsilon},\qquad C_\mu=0.09,$$

$$C_D=1.0,\qquad C_1=1.44(1+0.9R_f),\qquad C_2=1.92,$$

$$\sigma_k=1.0,\qquad \sigma_\varepsilon=1.3,\qquad R_f=\frac{2\nu_t(W-\omega r)\partial(W/r)/\partial r}{G}.$$

averaged Navier–Stokes equations. The Reynolds stresses are modelled using a modified $k$–$\varepsilon$ turbulence model to account for the swirling effect of the propeller.[6] The general form of the governing equations expressed in the rotating cylindrical co-ordinate system $(x, r, \theta)$ with constant angular velocity $\omega$ can be written as

$$\frac{\partial}{\partial x}(U\phi)+\frac{1}{r}\frac{\partial}{\partial r}(rV\phi)+\frac{1}{r}\frac{\partial}{\partial\theta}(W\phi)=\frac{\partial}{\partial x}\left(\Gamma_\phi\frac{\partial\phi}{\partial x}\right)+\frac{1}{r}\frac{\partial}{\partial r}\left(r\Gamma_\phi\frac{\partial\phi}{\partial r}\right)+\frac{1}{r}\frac{\partial}{\partial\theta}\left(\Gamma_\phi\frac{\partial\phi}{\partial\theta}\right)+S_\phi, \tag{1}$$

where $\phi$, $\Gamma_\phi$, and $S_\phi$ denote the flow variables, diffusion coefficients and source terms respectively as given in Table I.

## 3. TRANSFORMATION OF THE GOVERNING EQUATIONS

The flow domain is bounded by the blade passage, propeller hub, inlet and outlet sections and outer boundary plane. The non-orthogonal boundary-fitted co-ordinate system $(\xi, \eta, \zeta)$ is used to transform the physical domain into a rectangular computational domain. The transformation of the independent variables in the governing equations, leaving the flow variables $\phi$ in the original cylindrical co-ordinates, can be expressed as

$$\begin{aligned}\frac{\partial}{\partial\xi}(G^1\phi)+\frac{\partial}{\partial\eta}(G^2\phi)+\frac{\partial}{\partial\zeta}(G^3\phi)=&\frac{\partial}{\partial\xi}\left(\frac{\Gamma_\phi}{J}B_1^1\frac{\partial\phi}{\partial\xi}\right)+\frac{\partial}{\partial\eta}\left(\frac{\Gamma_\phi}{J}B_2^2\frac{\partial\phi}{\partial\eta}\right)+\frac{\partial}{\partial\zeta}\left(\frac{\Gamma_\phi}{J}B_3^3\frac{\partial\phi}{\partial\zeta}\right)\\&+\frac{\partial}{\partial\xi}\left(\frac{\Gamma_\phi}{J}B_2^1\frac{\partial\phi}{\partial\eta}\right)+\frac{\partial}{\partial\eta}\left(\frac{\Gamma_\phi}{J}B_3^2\frac{\partial\phi}{\partial\zeta}\right)+\frac{\partial}{\partial\zeta}\left(\frac{\Gamma_\phi}{J}B_1^3\frac{\partial\phi}{\partial\xi}\right)\\&+\frac{\partial}{\partial\xi}\left(\frac{\Gamma_\phi}{J}B_3^1\frac{\partial\phi}{\partial\zeta}\right)+\frac{\partial}{\partial\eta}\left(\frac{\Gamma_\phi}{J}B_1^2\frac{\partial\phi}{\partial\xi}\right)+\frac{\partial}{\partial\zeta}\left(\frac{\Gamma_\phi}{J}B_2^3\frac{\partial\phi}{\partial\eta}\right)+JS_\phi \quad (2)\end{aligned}$$

where the $B_i^j$ are elements of the transformation matrix represented by the partial derivatives of $(x, r, \theta)$ with respect to $(\xi, \eta, \zeta)$, $J$ is the Jacobian, the $G^i$ are contravariant velocity components and $S_\phi$ represents the source terms in the governing equations.

## 4. BOUNDARY CONDITIONS

The boundary conditions imposed on each boundary are as follows.

1. *Inlet section.* Uniform and inviscid flow conditions are used:

$$U = U_o, \qquad V = 0, \qquad W = \omega r, \qquad k = \varepsilon = 0. \quad (3)$$

2. *Outlet section.* Streamwise gradients of the flow variables are set to zero:

$$\frac{\partial U}{\partial\xi} = \frac{\partial V}{\partial\xi} = \frac{\partial W}{\partial\xi} = \frac{\partial k}{\partial\xi} = \frac{\partial\varepsilon}{\partial\xi} = 0. \quad (4)$$

3. *Blade and hub surfaces.* To avoid the difficulty in resolving the near-wall turbulent flow, the wall function method is employed. The first grid points next to the wall are placed in the logarithmic-law region ($30 \leq y^+ \leq 250$) and correlations of the wall function[7] are imposed.
4. *External boundary.* Uniform and inviscid flow conditions are assumed:

$$U = U_o, \qquad W = \omega R_e, \qquad k = \varepsilon = 0, \qquad P = P_o, \quad (5)$$

   where $R_e$ is the radius of the external boundary plane. The radial velocity at the edge of the external boundary is determined from the continuity equation.
5. *Periodic surfaces.* Periodic boundary conditions are given on the periodic surfaces.
6. *Wake centreline.* The boundary conditions at the wake centreline are specified by

$$\frac{\partial U}{\partial\eta} = \frac{\partial k}{\partial\eta} = \frac{\partial\varepsilon}{\partial\eta} = 0, \qquad V = W = 0. \quad (6)$$

## 5. NUMERICAL SCHEME

The governing equations are solved by the finite volume method.[8] A set of discretized equations is obtained by integrating the governing equations over the individual control volumes in the staggered

grid system,[8] where scalar variables are located at each grid node, while velocity components are placed between the scalar nodes. Convection terms are treated using a hybrid numerical scheme. Since the velocity field at each iteration does not satisfy the continuity equation, the velocity components are modified using the corrected values of the pressure which are determined to satisfy the continuity equation, i.e. the SIMPLE algorithm.[8] The final form of the discretized governing equations can be expressed as

$$a_P\phi_P = a_D\phi_D + a_U\phi_U + a_N\phi_N + a_S\phi_S + a_E\phi_E + a_W\phi_W + \overline{S_\phi}, \tag{7}$$

where the subscripts $P$, $D$, $U$, etc., refer to grid nodes.

## 6. CALCULATION

### *Propeller model*

The present numerical method is applied to calculate the DTRC 4119 propeller model with uniform flow conditions. As noted previously, Jessup[4] carried out extensive experiments for the present model using an LDV system in the water channel and provided substantial measured data on the pressure and velocity in the flow field. The 4119 propeller is a 12 inch diameter, three-blade propeller of relatively simple geometry. The propeller has a nearly constant pitch with no skew or rake. Each blade has NACA 66 section thickness form. In the experiment the advance ratio and the Reynolds number based on the chord length at 0·7 propeller radius are adjusted to 0·833 and $10^6$ respectively.

### *Computational grid*

The computational grid is algebraically generated for the calculation domain of the one-blade passage. The inlet boundary plane is placed at $x/D = -2{\cdot}0$, i.e. two diameters upstream of the propeller, while the outlet boundary plane is at $x/D = 3{\cdot}0$, i.e. three diameters downstream of the propeller. In the experiments of Jessup[4] the external boundary of the test section was located around $r/D = 1{\cdot}0$, but the external boundary plane in the present calculation is placed as far as three diameters from the hub axis to impose the uniform flow condition. Two types of grid are tested to investigate the effect of grid refinement. The coarse grid has $(\xi, \eta, \zeta)$ = (80,32,36) grid points and the fine grid has $(\xi, \eta, \zeta)$ = (95,45,46) grid points. Fine grid spacings are used near the leading and trailing edges of the blade, the blade and hub wall surfaces and the blade tip. Plane views of the computational grid for the fine grid system are shown in Figures 2 and 3.

Solutions are assumed to be converged when the residuals of the discretized equation are reduced to 1% of the maximum value. The convergence histories of the residuals for the fine grid are shown in Figure 4. The solutions converge after about 1000 iterations, which requires 80 h of computing time on an IBM 486 personal computer. Figure 5 shows calculation results for the pressure coefficient obtained with the coarse and fine grids. The two grids yield nearly identical results and no significant difference due to the grid refinement can be found. In the following discussion the calculations with the fine grid only are considered.

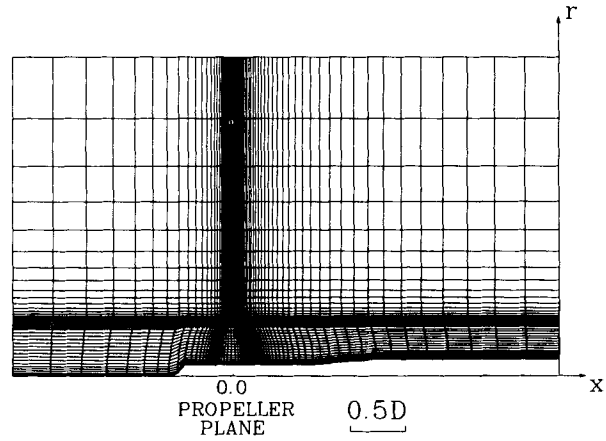


Figure 2. Plane view of generated numerical grid in $\zeta = 1$ plane

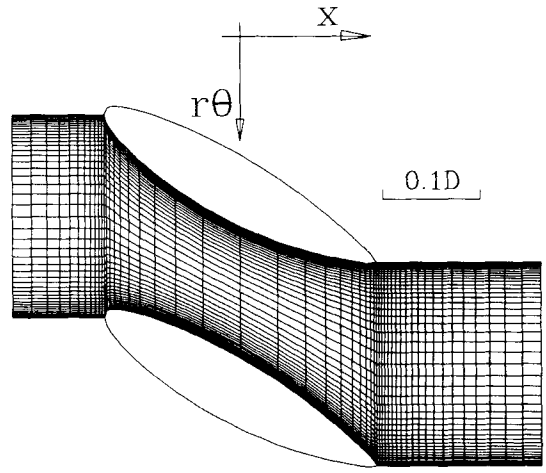


Figure 3. Partial view of numerical grid in $\eta = 1$ plane

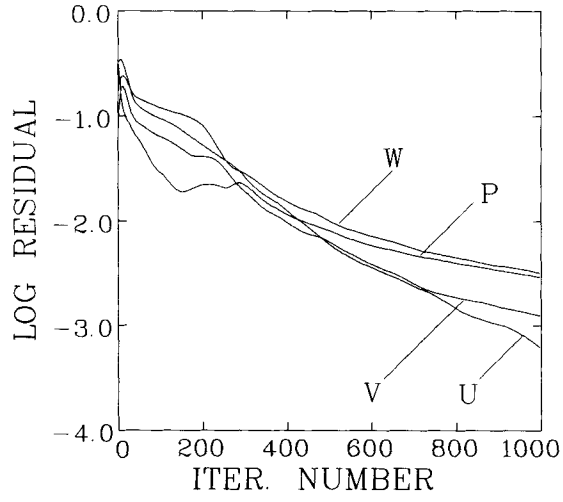


Figure 4. Convergence histories of residuals

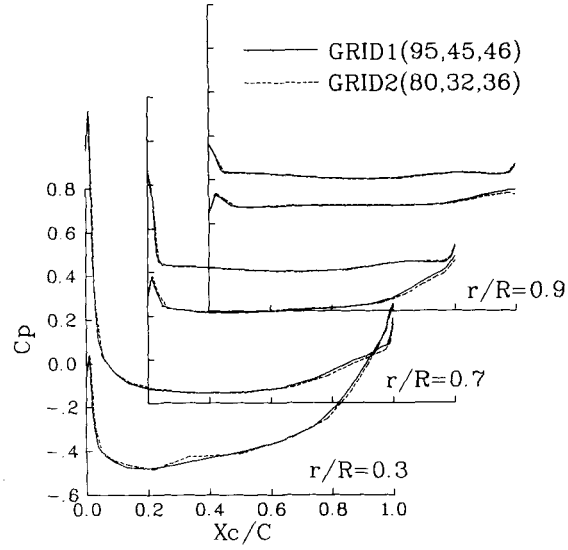


Figure 5. Grid dependence tests

*Results and discussion*

Figure 6 shows the circumferentially averaged axial and radial velocity distributions at $x/R = -0{\cdot}3$ near the inlet of the propeller. The axial flow acceleration due to the loading of the propeller is observed in the propeller disc as having a maximum value around 0·7 propeller radius. In the radial velocity profile a large outward motion can be seen near the hub and the radial flow direction is sharply reversed at the location of maximum flow acceleration. The prediction of the axial velocity shows reasonable agreement with the measurement, but the variations in the radial velocity are underpredicted.

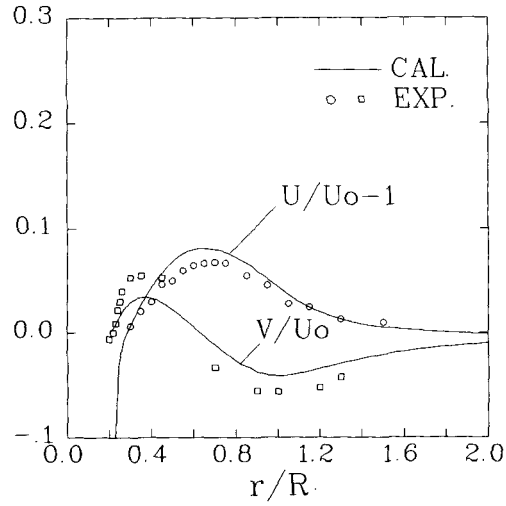


Figure 6. Circumferentially averaged axial and radial velocity profiles at $x/R = -0{\cdot}3$

Figures 7 and 8 show the circumferentially averaged velocity distributions at two axial planes in the slipstream of the propeller wake. The first one is close to the blade and the second one is at the end of the transition wake region where the wake starts to have a similar and final form. The swirling velocity component is defined in the fixed frame co-ordinate system as $W_s = \omega r - W$. In the slipstream of the propeller wake the flow is axially and tangentially accelerated owing to the propeller effect. The axial velocity becomes higher than the freestream velocity and the tangential velocity is much generated near the hub as decreasing radially outwards. The radial velocity becomes negative owing to the contraction of the slipstream. The predictions show satisfactory agreement with the measurements.

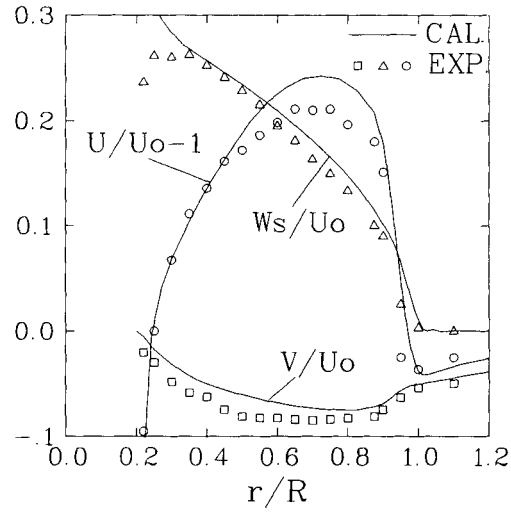


Figure 7. Circumferentially averaged velocity profiles at $x/R = 0{\cdot}328$

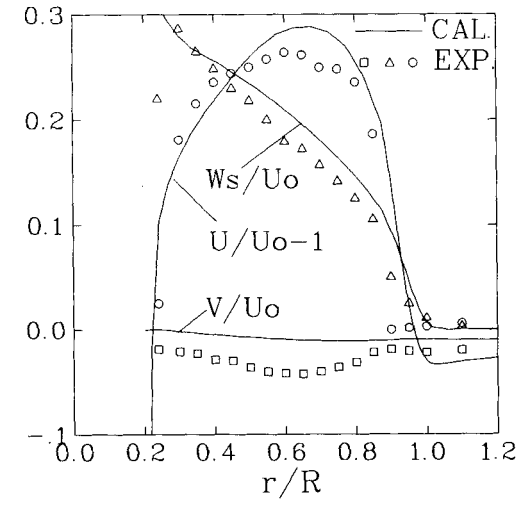


Figure 8. Circumferentially averaged velocity profiles at $x/R = 0{\cdot}951$

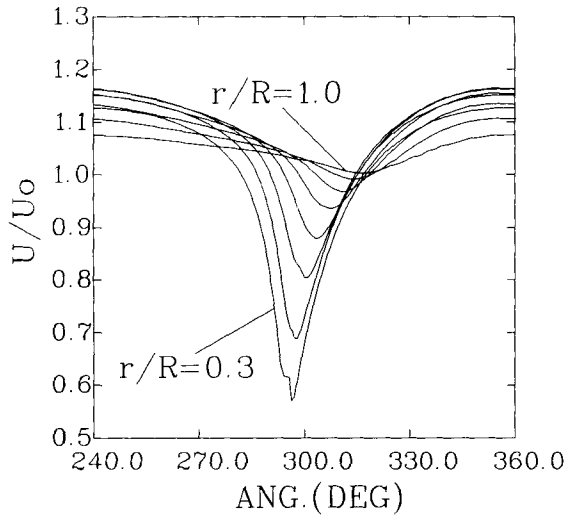


Figure 9. Circumferential variations in axial velocity at $x/R = -0{\cdot}3(r/R = 0{\cdot}3, 0{\cdot}4, 0{\cdot}5, 0{\cdot}6, 0{\cdot}7, 0{\cdot}8, 0{\cdot}9, 1{\cdot}0)$

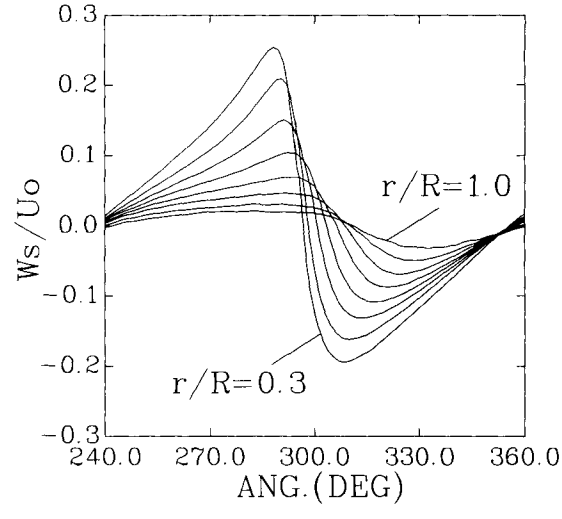


Figure 10. Circumferential variations in swirling velocity at $x/R = -0{\cdot}3(r/R = 0{\cdot}3, 0{\cdot}4, 0{\cdot}5, 0{\cdot}6, 0{\cdot}7, 0{\cdot}8, 0{\cdot}9, 1{\cdot}0)$

However, the calculations slightly overpredict the axial velocity in the wake cores and do not show the sharp variations in the tangential velocity near the hub.

The propeller flow characteristics can be identified via the periodic variations in the flow variables in the blade passage. The variations in the axial and swirling velocities near the inlet of the propeller are shown in Figures 9 and 10 respectively. The angular position is adjusted so that the front of the blade is located at around 300°. The flow field appears to be significantly influenced by the blade. The blade effect is largest near the hub where the section of the blade is relatively thick. The axial velocity decreases sharply, resulting in a velocity defect around the blade position, which is due to the stagnation point around the leading edge. The direction of the tangential velocity changes rapidly from positive on the pressure side to negative on the suction side as one goes through the blade.

To investigate the tip vortex generation, the distributions of the pitchline component of the vorticity near the tip are shown in Figure 11. The pitchline component of the vorticity is defined as

$$\omega_P = \frac{W_P}{r} - \frac{1}{r \sin \phi_P} \frac{\partial V_P}{\partial \theta} + \frac{\partial W_P}{\partial r}, \tag{8}$$

where

$$V_P = V, \tag{9}$$

$$W_P = -U \cos \phi_P + W \sin \phi_P \tag{10}$$

and $\phi_p$ is the pitch angle of the blade. The vortex flow pattern can be seen around the same location as observed in the measurement. However, the tip vortex is weakly predicted and the predicted pitchline vorticity in the vortex core is much less than the measured one. Figure 12 shows the trajectory of the tip vortex core along the axial distance. It is seen that the radial position of the tip vortex is displaced in the near wake and reaches its final value at one radius downstream of the propeller. The predictions show a similar trend, but the predicted radial positions are somewhat higher than the measured ones.

The pressure coefficient distributions on the pressure and suction sides of the blade at $r/R = 0{\cdot}3$, 0·7 and 0·9 are shown in Figure 13. The predictions are in good agreement with the measurements at

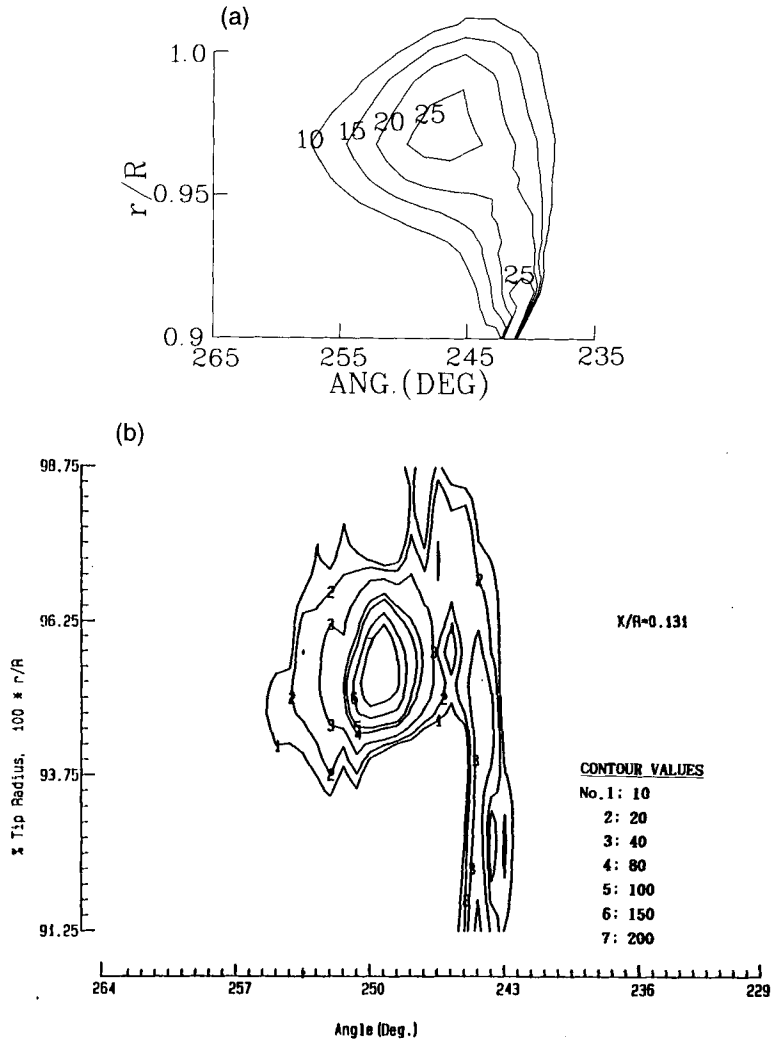


Figure 11. Contours of pitchline component of vorticity at $x/R = 0{\cdot}13$: (a) calculation, $\omega_P R/U_o = 10, 15, 20, 25$; (b) experiment[4], $\omega_P R/U_o = 10, 20, 40, 80, 100, 150, 200$

$r/R = 0{\cdot}7$ but show relatively poor agreement in the after-chord region of 0·3 and 0·9 radius, where the hub or tip vortex may distort the flow field.

In propeller flow with uniform flow conditions, viscous effects are confined to a small region of the boundary layer. Jessup[4] provided two measured data sets of the boundary layer for the smooth blade and the tripped blade with leading edge roughness. Measurements were made for the tripped blade to investigate the turbulent boundary layer of the real-scale propeller, since laminar boundary layers develop on a large portion of the blade in the case of the model-scale propeller. In the present calculation the flow is assumed to be turbulent in the overall region of the blade, since there is no available turbulence model to reflect the laminar and transitional flow. It is also noted that only a few grid points are placed in the boundary layer region, because a sufficient number of grid point cannot be provided in the small region of the boundary layer. Figure 14 shows the pitchline velocity distributions

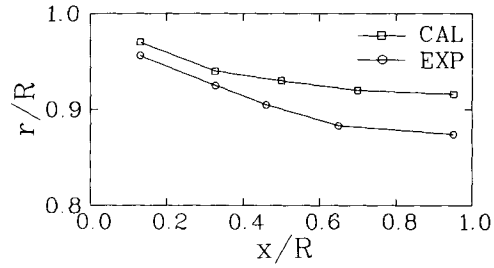


Figure 12. Radial location of tip vortex core

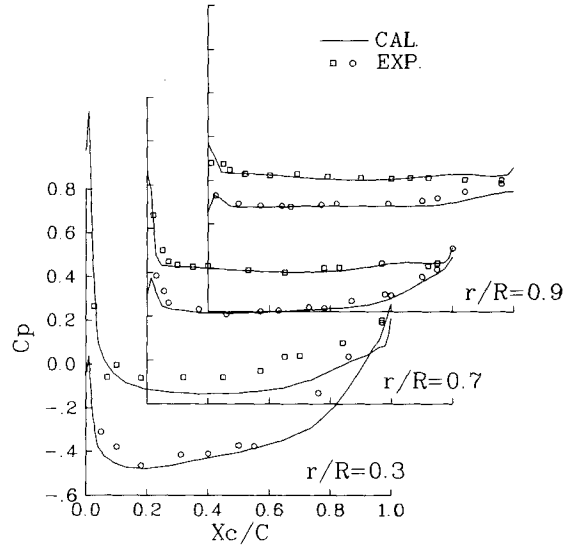


Figure 13. Pressure coefficient distributions along pressure and suction sides at $r/R = 0{\cdot}3, 0{\cdot}7$ and $0{\cdot}9$

in normal directions on the suction-side wall of the blade at 0·7 radius, where the pitchline velocity is derived using the definition

$$U_P = U \sin \phi_P + W \cos \phi_P \tag{11}$$

and normalized by the resultant inflow velocity $U_R$. It can be seen that the laminar boundary layer develops up to 0·6 chord for the smooth blade, while the boundary layer undergoes a transition at 0·2 and 0·3 chord and becomes turbulent after 0·5 chord for the tripped blade. In the laminar and transition region, measured profiles are not represented in the prediction, since the flow is assumed to be turbulent. However, the predictions show satisfactory agreement with the measurements in the turbulent boundary layer region and it is indicated that the turbulent boundary layer at 0·7 chord is similar to the equilibrium boundary layer following the logarithmic law of the wall.

Finally, the thrust and torque of the propeller are estimated for a wide range of advance coefficients, including off-design conditions. The thrust and torque coefficients for the DTRC 4119 propeller were measured in an open water test.[4] The hub configuration for this test was slightly different from the hub shape used in the experiment of Jessup and calculation is performed again for the model tested in open water. Figure 15 shows the thrust and torque coefficients compared with the measured data in the open

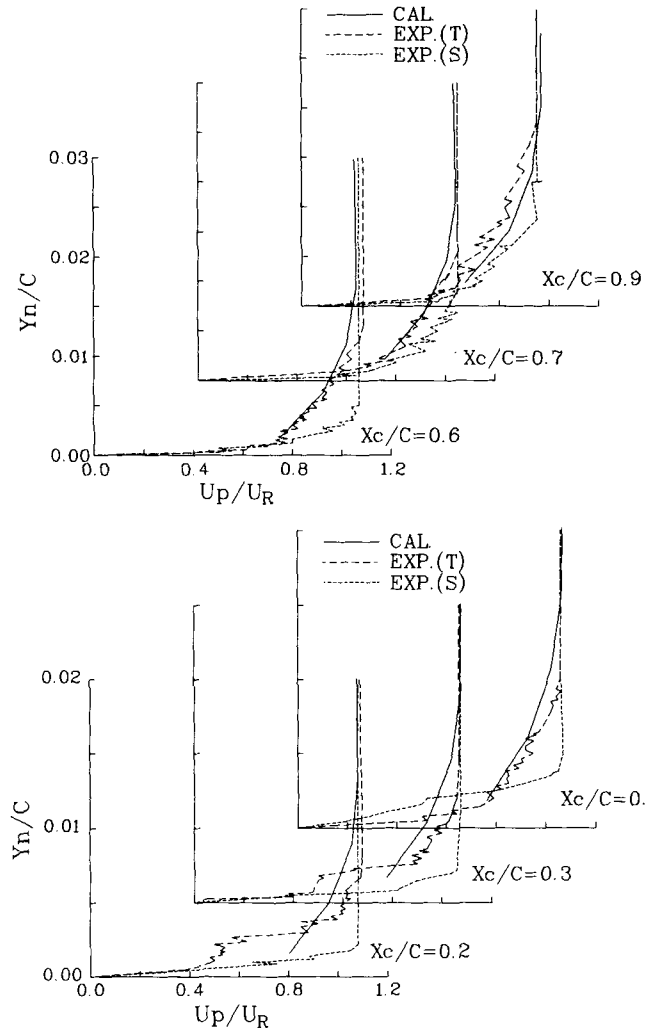


Figure 14. Boundary layer profiles on suction side at $r/R = 0{\cdot}7$

water tests. The estimations show reasonable agreement but slightly overpredict the thrust and torque, the largest difference occurring for the low advance coefficient $J = 0{\cdot}5$. The difference seems to be due to the free surface effect in the open water tests. Comparisons show that the free surface effect becomes relatively large for low advance coefficients.

## 7. CONCLUSIONS

A numerical method is developed to calculate propeller flow and applied to a model propeller operating in a uniform flow. The general features of propeller flow can be reasonably predicted and the predictions are in good agreement with measurements of the velocity and pressure in the flow field. The tip vortex flow pattern can be reproduced near the tip, but the magnitude of the vorticity in the vortex core is much less than the measured one. The calculated boundary layer profiles show good

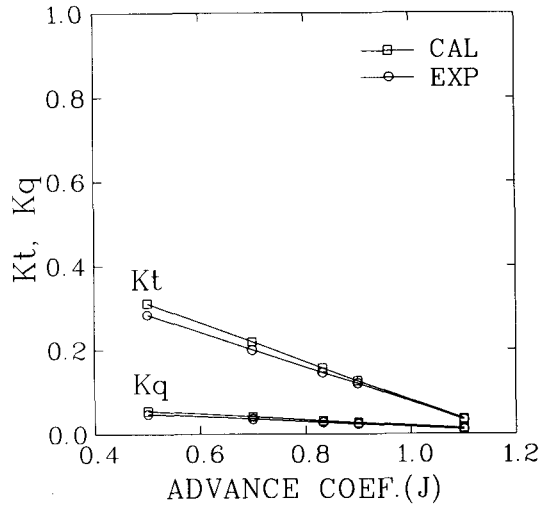


Figure 15. Comparison of estimated thrust and torque coefficients with measured data

agreement with those measured in the turbulent boundary layer region at 0·7 propeller radius, but the laminar and transitional boundary layers cannot be represented, because the flow is assumed to be turbulent in the calculation. The thrust and torque coefficients can be estimated for a wide range of advance coefficients, including off-design conditions, and the estimated values are in reasonable agreement with open water test data.

Acknowledgement

This research was supported by the Korea Science and Engineering Foundation under contract 931-1000-038-1.

REFERENCES

1. F. Stern, H. T. Kim, V. C. Patel, H. C. Chen, 'A viscous flow approach to the computation of propeller hull interaction', *J. Ship Res.* **32**, 246–262 (1988).
2. F. Stern, H. T. Kim, 'Computation of viscous flow around a propeller-shaft configuration with infinite-pitch rectangular blades', *Proc. 5th Int. Conf. on Numerical Ship Hydrodynamics*, Hiroshima, 1990, pp. 408–423.
3. H. T. Kim, 'Navier–Stokes computation of incompressible propeller flowfield', *Proc. 2nd Japan–Korea Joint Workshop on Ship and Marine Hydrodynamics*, Osaka, 1993, pp. 9–22.
4. S. D. Jessup, 'An experimental investigation of viscous aspects of propeller blade flow', *Ph.D. Thesis*, Catholic University of America, Washington, D. C, 1989.
5. B. S. Hyun, 'Measurements in the flow around a marine propeller at the stern of an axisymmetric body', *Ph.D. Thesis*, University of Iowa, 1990.
6. M. A. Leschziner and W. Rodi, 'Computation of strongly swirling axisymmetric free jets', *AIAA J.* **22**, 1742–1747 (1983).
7. A. D. Gosmann and F. J. K. Ideriah, *TEACH-2E Computation Code Manual*, Department of Mechanical Engineering, Imperial College, London, 1976.
8. S. V. Patankar, *Numerical Heat Transfer and Fluid Flow*, McGraw-Hill, New York, 1980.